DOI 10.1007/s11182-023-03062-4
Russian Physics Journal, Vol. 66, No. 11, January, 2024

CONSTRUCTION OF A TWO-DIMENSIONAL DISCRETE DISLOCATION MODEL TO DESCRIBE THE PLASTIC DEFORMATION PROCESS OF A SINGLE CRYSTAL

N. A. Knyazev and P. S. Volegov UDC 539.3

The paper considers the development and numerical implementation of a two-dimensional discrete dislocation model to describe the inelastic deformation of a hexagonal close-packed (HCP) single crystal, taking into account long-range and short-range dislocation interactions. The analytical results are obtained for image fields using the Fourier series for cases of dislocation approaching the crystal boundaries. The model adequacy tests are carried out, and the evolution of the dislocation structure is illustrated with the gradual inclusion of the mechanisms of dislocation annihilation, dislocation pinning at obstacles, and dislocation nucleation by the Frank-Read sources.

Keywords: Dislocation structure, image fields, finite element method, HCP single crystal.

INTRODUCTION

Metal products with the desired shape and required physical and mechanical properties are manufactured by various methods of metal processing, including metal forming. The key factor in the metal forming application is the implementation of the plastic deformation process, which results in a change in the internal structure of the material and consequently, its physical and mechanical properties. The continuous emergence of new materials, the development of special metalworking regimes, and the high production quality requirements for the manufactured products are the main reasons to study the plasticity phenomenon and understand the nature of plastic deformation.

The dislocation motion in metals and alloys is currently the main mechanism of plastic deformation [1]. Already at the initial stage of plasticity, there is a qualitative change in the momentum transfer mechanism due to the dislocation movement in the elastic stress fields [2]. Further interaction of dislocations with each other and with other defects of the crystal lattice largely depends on the prescribed deformation conditions and the crystalline material structure and plays a decisive role in establishing its mechanical response.

To analyze the dislocation structures, a pattern of the appearance of material regions with high and low dislocation densities that have a relatively clear periodicity in the micrometer range (cells, subgrains, walls, channels, etc.) is often used [3]. To distinguish the inhomogeneity of distributions of dislocations of different types in a material, a classification of dislocation structures is used. In [4, 5], the following dislocation structure types were considered: random dislocation distribution, pile-ups, tangles, networks, slip bands, cells, and fragments. In the plastic deformation process, the predominance of some plasticity mechanisms over others can cause a change in the dislocation structure type. For example, an initially homogenous dislocation structure with low stacking fault energy (SFE) can be transformed into a structure with pile-ups. When activating multiple slip systems, another transition to the dislocation network structure is possible.

It was noted in [6] that high-temperature deformation leads to the formation of low-energy cellular structures, which was confirmed experimentally [7]. This is due to the intensive work of thermally activated dislocation climb and cross-slip mechanisms, as a result of which the total dislocation density decreases due to the dislocation annihilation

Perm National Research Polytechnic University, Perm, Russia, e-mail: nikita.kniaziev@mail.ru; crocinc@mail.ru. Original article submitted October 27, 2023.

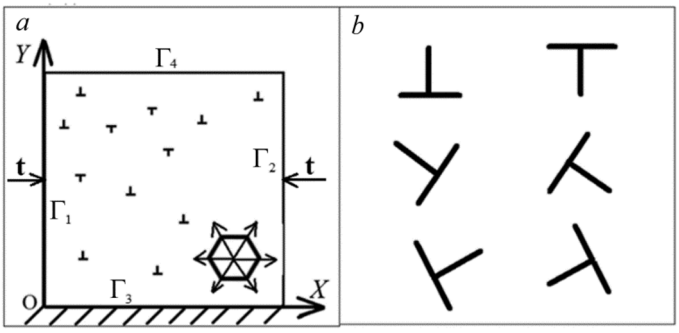

Fig. 1. Schematic representation of the dislocation movement in six different directions (*a*) and six types of dislocation gliding in prismatic slip systems of HCP titanium (*b*).

process. A decrease in the dislocation density at elevated temperatures promotes the formation of low-angle cell or subgrain boundaries. An important role in the dislocation self-organization processes is played by the stacking fault energy. It is well known that in metals and alloys with a low SFE, flat dislocation pile-ups are usually formed, which transform into a dislocation network structure in multislip conditions [8]. In turn, the dislocation structure of materials with high SFE is most often tangled and cellular. When cyclic loads occur, the dislocation structure is transformed into low-energy, stable configurations. Researchers observe the formation of multiple prismatic loops that turn into persistent slip bands under intense inelastic deformation at a low cyclic deformation amplitude [9]. High deformation amplitude leads to the appearance of dislocation walls in the material structure.

Thus, there are patterns of dislocation structure formation in a material that need to be investigated. The main problem with experimental studies is that the location of dislocations in the material is obtained only after sample loading. In addition, in most experimental works, information about the dislocation dynamics or the evolution of the dislocation structure during plastic deformation is lacking. An effective way to study the dislocation structure dynamics is to develop mathematical models. Recently, discrete dislocation models have become widespread. The main feature of the discrete dislocation approach is the explicit consideration of the dislocation motion and interaction (annihilation, nucleation by Frank–Read sources, formation of junctions and dipoles, cross-slip, etc.) to describe the evolution of the dislocation structure of the material.

In this work, we construct a two-dimensional discrete dislocation dynamics model to describe the inelastic deformation of an HCP single crystal, which makes it possible to study the evolution of the dislocation structure and takes into account the influence of the free surface. A review of two-dimensional models showed their successful applicability to describe the processes of plastic deformation [10], nano- and microindentation [11, 12], and fracture of single crystals and polycrystals [13, 14]. It should be noted that three-dimensional discrete models consider more complex mechanisms of the curved dislocation interaction (cross-slip, formation of junctions, kinks, jogs, etc.) [15], but this is a more resource-intensive task.

MODEL DESCRIPTION

To describe the dislocation structure evolution of a single crystal, we introduce the hypothesis of considering pure edge dislocations of different signs in the two-dimensional case. Dislocation slip is the main mechanism of dislocation motion. The dislocation climbing mechanism is not included in the consideration due to the slow and low-temperature deformation of the crystal. If we compare the plane in which dislocations move with the basal plane of the hexagonal close-packed (HCP) titanium lattice, then the dislocation movement can go in six different directions (Fig. 1*a*). These directions correspond to the three prismatic slip systems of HCP titanium, which are primary and dominant in the material. Thus, there are only six types of edge dislocations in the model (Fig. 1*b*).

At the initial time, dislocations are uniformly distributed throughout the crystal, and then they begin to slide according to the equations [9]:

$$\tau^i = \frac{1}{b^2}\left\{(b^i \cdot \sigma^i) \times l^i\right\} \cdot b^i,$$

$$\tau^i_{eff} = \left(\tau^i - \text{sign}\left(\tau^i\right)\tau_{fr}\right) H\left(\tau^i - \tau_{fr}\right),$$

$$V^i = \frac{\tau^i_{eff}\, b^i}{B},$$

$$\frac{\partial X^i}{\partial t} = V^i,$$

$$i = 1,..,N,$$

where b^i and l^i are the Burgers vector and the unit vector tangent to the dislocation line, V^i is the dislocation velocity vector, σ^i is the total stress field acting on the ith dislocation, B is the phonon drag coefficient, τ^i_{eff} is the effective shear stress, τ_{fr} is the lattice friction (Peierls) stress, and H is the Heaviside function. When the acting shear stresses exceed the Peierls stress, the dislocation begins to move in the corresponding slip direction, which depends on the dislocation type.

To calculate the total stress field, it is necessary to consider the internal dislocation stresses and the externally applied stresses. In order to achieve this, based on work [16], we divide the total stress, displacement, and deformation fields into two components:

$$u = \tilde{u} + \hat{u}, \quad \varepsilon = \tilde{\varepsilon} + \hat{\varepsilon}, \quad \sigma = \tilde{\sigma} + \hat{\sigma}\,. \tag{1}$$

The components $\tilde{u}, \tilde{\varepsilon}$, and $\tilde{\sigma}$ are superpositions of the corresponding dislocation fields. The field of stresses, displacements, and deformations for a single edge dislocation located in an infinitely large isotropic elastic medium has the form [17]:

$$\sigma_{11} = \frac{-Gb}{2\pi(1-\nu)}\frac{y'(3x'^2 + y'^2)}{(x'^2 + y'^2)^2}, \sigma_{22} = \frac{Gb}{2\pi(1-\nu)}\frac{y'(x'^2 - y'^2)}{(x'^2 + y'^2)^2},$$

$$\sigma_{12} = \frac{Gb}{2\pi(1-\nu)}\frac{x'(x'^2 - y'^2)}{(x'^2 + y'^2)^2},$$

$$u_1 = \frac{b}{2\pi}\left[\arctan\left(\frac{y'}{x'}\right) + \frac{x'y'}{2(1-\nu)(x'^2 + y'^2)}\right], \tag{2}$$

$$u_2 = -\frac{b}{2\pi}\left[\frac{1-2\nu}{4(1-\nu)}\ln\left(x'^2 + y'^2\right) + \frac{x'^2 - y'^2}{4(1-\nu)(x'^2 + y'^2)}\right],$$

$$\varepsilon_{11} = \frac{\partial u_1}{\partial x'}, \varepsilon_{22} = \frac{\partial u_2}{\partial y'}, \varepsilon_{12} = \frac{1}{2}\left(\frac{\partial u_1}{\partial y'} + \frac{\partial u_2}{\partial x'}\right),$$

where G is the shear modulus, ν is the Poisson ratio, b is the Burgers vector length, and x', y' are the point coordinates in the Cartesian coordinate system constructed as follows: the abscissa axis is directed along the dislocation Burgers vector, and the ordinate axis lies in the direction of the normal to the slip plane.

The solution above cannot be applied in the dislocation core region since in this place the stress, displacement, and deformation fields begin to increase infinitely. To solve the problem of the singularity of these fields near the dislocation core, the cutoff radius $r = 2a$ (a is the lattice parameter) is introduced, which forms the circular area where relations (2) are modified. It is proposed to modify these relations using the results presented in work [18], where the authors obtained the nonsingular solution for the stress field of an infinite edge dislocation.

Dislocations create a stress field at the boundaries of a single crystal with a finite volume, since analytical solution (2) was obtained in an infinite medium. The image fields $\hat{u}, \hat{\varepsilon}$, and $\hat{\sigma}$ in relation (1) allow getting rid of additional dislocation perturbations at the boundaries and ensure preserving the actual boundary conditions. To find image fields, the boundary value problem:

$$\nabla \cdot \hat{\boldsymbol{\sigma}} = \mathbf{0}, \; x \in \Omega,$$

$$\hat{\boldsymbol{\sigma}} = \mathbf{D} : \hat{\boldsymbol{\varepsilon}}, \; x \in \Omega,$$

$$\hat{\boldsymbol{\varepsilon}} = \frac{1}{2}\left(\nabla \hat{\mathbf{u}} + \hat{\mathbf{u}} \nabla\right), \; x \in \Omega,$$

$$\mathbf{n} \cdot \hat{\boldsymbol{\sigma}} = \hat{\mathbf{t}} = \mathbf{t} - \tilde{\mathbf{t}}, \; x \in \Gamma_t,$$

$$\mathbf{U} = \hat{\mathbf{u}} = \mathbf{u} - \tilde{\mathbf{u}}, \; x \in \Gamma_U$$

must be solved, where **t** and **u** are the actual surface loads and displacements, and **D** is the elasticity tensor. Thus, the total stress field σ is sensitive to a change in the dislocation structure of the material and includes the internal dislocation stresses. In this case, the actual boundary conditions are preserved due to the image field introduction.

In addition to long-range interactions, the model includes short-range dislocation interactions: dislocation annihilation, dislocation pinning at obstacles, and dislocation nucleation by the Frank–Read sources. The annihilation of two dislocations with opposite signs and the Burgers vectors occur at the critical distance $L_e = 6b$ [10, 12, 13]. Obstacles are modeled as fixed points with a given density ρ_{obs} in the crystal volume. The dislocation capture occurs at the critical distance r_{obs}, after which the pinned dislocation can overcome obstacles only if the force acting on the dislocation exceeds the threshold value (or $\tau_{eff}^{i} > \tau_{obs}$). The Frank–Read sources are also fixed points with a density ρ_{nuc}. In the case when the effective shear stress in the source area exceeds the critical value ($\tau_{eff} > \tau_{nuc}$), a dislocation pair is generated during the period of time t_{nuc}. To prevent the process of dislocation annihilation in a pair, it is necessary to arrange dislocations at a sufficient distance, not less than L_{nuc} [10].

PROBLEM OF DETERMINING THE IMAGE FIELDS

Works [19, 20] were aimed at solving the problem of using the finite element method (FEM) when a curved dislocation intersects a free surface. It was noted that the method could not efficiently calculate image fields in this case. So, when using a uniform mesh, the total number of nodes becomes impractically large before numerical convergence is achieved. In turn, the use of an adaptive mesh is also a difficult task: the mesh construction must be carried out at each time step and for many dislocations, which leads to high computational loads. In this paper, a boundary layer is introduced for each boundary to solve the problem. When dislocations enter the boundary layer, the procedure for image field calculation includes not only the FEM application, but also explicit modeling of image dislocations. For this, we considered various cases of dislocation location relative to the free boundary.

Consider the case of an edge dislocation location, the orientation of which is determined by the angle α, near the right boundary. The image dislocation is located relative to the original dislocation, as shown in Fig. 2. The components $\sigma_{xx}(0, y)$ and $\sigma_{yy}(0, y)$ of the stress field superposition of the initial dislocation and the image dislocation

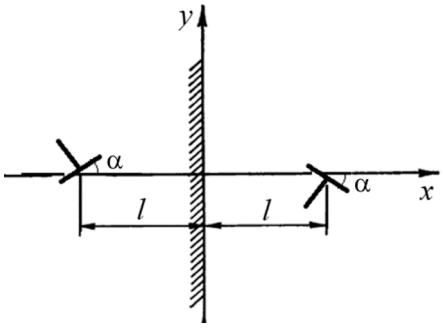

Fig. 2. Edge dislocation (left) and its corresponding image dislocation (right) near the free surface.

at the boundary have zero values. The component $\sigma_{xy}(0, y)$ at the boundary is not vanishing, and the expression for it takes the form:

$$\sigma_{xy}(0, y) = \frac{Gb}{\pi(1-\nu)}\left[\frac{(l\cos\alpha + y\sin\alpha)((l^2 - y^2)\cos 2\alpha + 2l\, y\sin 2\alpha)}{(l^2 + y^2)^2}\right]. \tag{3}$$

Therefore, the task is to find an additional stress field $\boldsymbol{\sigma}^{add}$, such that $\sigma_{xy}^{add}(0, y) = -\sigma_{xy}(0, y)$ and $\sigma_{xx}^{add}(0, y) = 0$ in the *xOy* plane.

Function (3) is not absolutely integrable, so we write the solution for the Airy stress function $\Psi(x, y)$ on the interval [–*T*, *T*] as a trigonometric series:

$$\Psi(x, y) = \sum_{n=1}^{\infty} X_n(x)\, Y_n(y) = \sum_{n=1}^{\infty}\left[X_n(x)\cos\lambda_n y + X_n(x)\sin\lambda_n y\right],\ \lambda_n = \pi n / T,$$

$$Y(y) = a\sin(\lambda y) + b\cos(\lambda y),$$

$$X(x) = (c_1 + c_2 x)e^{\lambda x} + (c_3 + c_4 x)e^{-\lambda x}.$$

Taking the boundary conditions

$$\psi(-\infty, y) \to 0 \Rightarrow c_3 = c_4 = 0,$$

$$\sigma_{xx}^{add}(0, y) = \frac{\partial^2\Psi(0, y)}{\partial y^2} = 0 \Rightarrow \frac{\partial^2 Y(y)}{\partial y^2}X(0) = 0 \Rightarrow X(0) = 0 \Rightarrow c_1 = 0,$$

we obtain:

$$\Psi(x, y) = A_0\, e^x y + \sum_{n=1}^{\infty}\left[A_\lambda x\, e^{\lambda x}\sin(\lambda y) + B_\lambda x\, e^{\lambda x}\cos(\lambda y)\right],$$

$$\frac{\partial^2\Psi(0, y)}{\partial x\,\partial y} = A_0 + \sum_{n=1}^{\infty}\left[A_\lambda\lambda\cos(\lambda y) - B_\lambda\lambda\sin(\lambda y)\right] = \sigma_{xy}(0, y) = -\sigma_{xy}^{add}(0, y). \tag{4}$$

Expression (4) is the Fourier series with coefficients A_0, A_λ, and B_λ :

$$A_0 = \frac{a_0}{2} = \frac{Gb}{\pi(1-\nu)}\left[\frac{\cos\alpha}{T}\left(\frac{lT(2\cos 2\alpha - 1)}{l^2+T^2} + 2\arctan\left(\frac{T}{l}\right)\sin^2\alpha\right)\right],$$

$$A_\lambda = \frac{1}{T\lambda}\int_{-T}^{T}\sigma_{xy}(0,y)\cos(\lambda y)\,dy = \frac{Gb}{\pi^2 n(1-\nu)}\int_{-T}^{T}\tilde{\sigma}_{xy}(0,y)\cos\left(\frac{\pi n}{T}y\right)dy,$$

$$B_\lambda = -\frac{1}{T\lambda}\int_{-T}^{T}\sigma_{xy}(0,y)\sin(\lambda y)\,dy = -\frac{Gb}{\pi^2 n(1-\nu)}\int_{-T}^{T}\tilde{\sigma}_{xy}(0,y)\sin\left(\frac{\pi n}{T}y\right)dy.$$

Using these coefficients, we obtain the general form of the Airy stress function and components of the additional stress field $\boldsymbol{\sigma}^{add}$ near the right boundary:

$$\sigma_{xy}^{add} = -A_0 e^{x} + \sum_{n=1}^{\infty}\left[-e^{\lambda x}\lambda(1+\lambda x)\left(A_\lambda\cos(\lambda y) - B_\lambda\sin(\lambda y)\right)\right],$$

$$\sigma_{xx}^{add} = \sum_{n=1}^{\infty}\left[-e^{\lambda x}\lambda^2 x\left(A_\lambda\sin(\lambda y) + B_\lambda\cos(\lambda y)\right)\right],$$

$$\sigma_{yy}^{add} = A_0\, e^{x} y + \sum_{n=1}^{\infty}\left[e^{\lambda x}\lambda(2+\lambda x)\left(A_\lambda\sin(\lambda y) + B_\lambda\cos(\lambda y)\right)\right].$$

Additional stress field components near the left, upper, and lower boundaries are calculated similarly (using expressions (5), (6), and (7), respectively):

$$\sigma_{xy}^{add} = A_0 e^{-x} + \sum_{n=1}^{\infty}\left[e^{-\lambda x}\lambda(-1+\lambda x)\left(A_\lambda\cos(\lambda y) - B_\lambda\sin(\lambda y)\right)\right],$$

$$\sigma_{xx}^{add} = \sum_{n=1}^{\infty}\left[-e^{-\lambda x}\lambda^2 x\left(A_\lambda\sin(\lambda y) + B_\lambda\cos(\lambda y)\right)\right], \tag{5}$$

$$\sigma_{yy}^{add} = A_0\, e^{-x} y + \sum_{n=1}^{\infty}\left[e^{-\lambda x}\lambda(-2+\lambda x)\left(A_\lambda\sin(\lambda y) + B_\lambda\cos(\lambda y)\right)\right],$$

$$\sigma_{xy}^{add} = -A_0 e^{y} + \sum_{n=1}^{\infty}\left[-e^{\lambda y}\lambda(1+\lambda y)\left(A_\lambda\cos(\lambda x) - B_\lambda\sin(\lambda x)\right)\right],$$

$$\sigma_{xx}^{add} = A_0\, e^{y} x + \sum_{n=1}^{\infty}\left[e^{\lambda y}\lambda(2+\lambda y)\left(A_\lambda\sin(\lambda x) + B_\lambda\cos(\lambda x)\right)\right], \tag{6}$$

$$\sigma_{yy}^{add} = \sum_{n=1}^{\infty}\left[-e^{\lambda y}\lambda^2 y\left(A_\lambda\sin(\lambda x) + B_\lambda\cos(\lambda x)\right)\right],$$

$$\sigma_{xy}^{add} = A_0 e^{-y} + \sum_{n=1}^{\infty}\left[e^{-\lambda y}\lambda(-1+\lambda y)\left(A_\lambda \cos(\lambda x) - B_\lambda \sin(\lambda x)\right)\right],$$

$$\sigma_{xx}^{add} = A_0\, e^{-y} x + \sum_{n=1}^{\infty}\left[e^{-\lambda y}\lambda(-2+\lambda y)\left(A_\lambda \sin(\lambda x) + B_\lambda \cos(\lambda x)\right)\right], \quad (7)$$

$$\sigma_{yy}^{add} = \sum_{n=1}^{\infty}\left[-e^{-\lambda y}\lambda^2 y\left(A_\lambda \sin(\lambda x) + B_\lambda \cos(\lambda x)\right)\right].$$

Thus, the stress field superposition of the initial dislocation, image dislocation, and additional stress field results in zero shear and normal stresses at the boundaries of the single crystal.

RESULTS

The simulated single crystal had a square shape with side lengths of $5\,\mu$m (5000 nm) in the two-dimensional case. The loading conditions corresponded to uniaxial compression of the titanium sample with a given stress vector **t** directed along the *X* axis (Fig. 1*a*). The lower boundary was rigidly fixed, and the upper boundary was free. So, the boundary conditions on the surface Γ_1, Γ_2, Γ_3, and Γ_4 take the form:

$$\Gamma_1 : (\boldsymbol{\sigma}\cdot\mathbf{n}_1)_x = t,\ (\boldsymbol{\sigma}\cdot\mathbf{n}_1)_y = 0,$$

$$\Gamma_2 : (\boldsymbol{\sigma}\cdot\mathbf{n}_2)_x = -t,\ (\boldsymbol{\sigma}\cdot\mathbf{n}_2)_y = 0,$$

$$\Gamma_3 : u_x^3 = 0,\ u_y^3 = 0, \quad (8)$$

$$\Gamma_4 : (\boldsymbol{\sigma}\cdot\mathbf{n}_4)_x = 0,\ (\boldsymbol{\sigma}\cdot\mathbf{n}_4)_y = 0.$$

To verify that the method for determining the image fields works correctly when dislocations enter the boundary layer, a numerical experiment was conducted. For this purpose, several dislocations of different types were placed in the boundary layer near the upper free boundary (Fig. 3*a*). The component σ_{22} on the upper boundary takes a zero value due to the fields of image dislocations located in a special way on the other side of the boundary. To eliminate the shear component σ_{12}, we discussed the issue of introducing an additional stress field $\boldsymbol{\sigma}^{add}$ in the previous chapter. The shear component distributions of the dislocation stress field (superposition of the initial and image dislocation fields) and the additional stress field are plotted in Fig. 3*b*. As a result, the total stress field has zero normal and shear components at the upper boundary.

In further numerical experiments, the following values of the model parameters were used: $t = 300$ MPa, $G = 39.5$ GPa [13], $\nu = 0.33$ [13], $b = 0.32$ nm [13], $B = 10^{-4}$ Pa·s [13, 14], $\tau_{fr} = 19.72$ MPa [9], $L_e = 6b$ [10, 13], $r_{obs} = 70b$, $\rho_{obs} = 3\cdot 10^9$ cm^{-2}, $\rho_{nuc} = 5\cdot 10^8$ cm^{-2}, $\tau_{obs} = 228$ MPa [10], $\tau_{nuc} = 76$ MPa [10], $L_{nuc} = 125b$ [10], and $t_{nuc} = 10$ ns. The values of most parameters were taken from the known discrete dislocation models, and some parameters (such as obstacles and density of sources) were set independently. Initial dislocation distribution in the single crystal was uniform, the single crystal loading scheme and the crystal sizes remained unchanged.

The distributions of the dislocation stress field components, image stress field, and total stress field on the left, right, and upper single crystal boundaries are plotted in Fig. 4. It can be seen that the normal stresses on the left and right boundaries coincide in magnitude with the compressive load value *t*, while the upper boundary remains free from stresses.

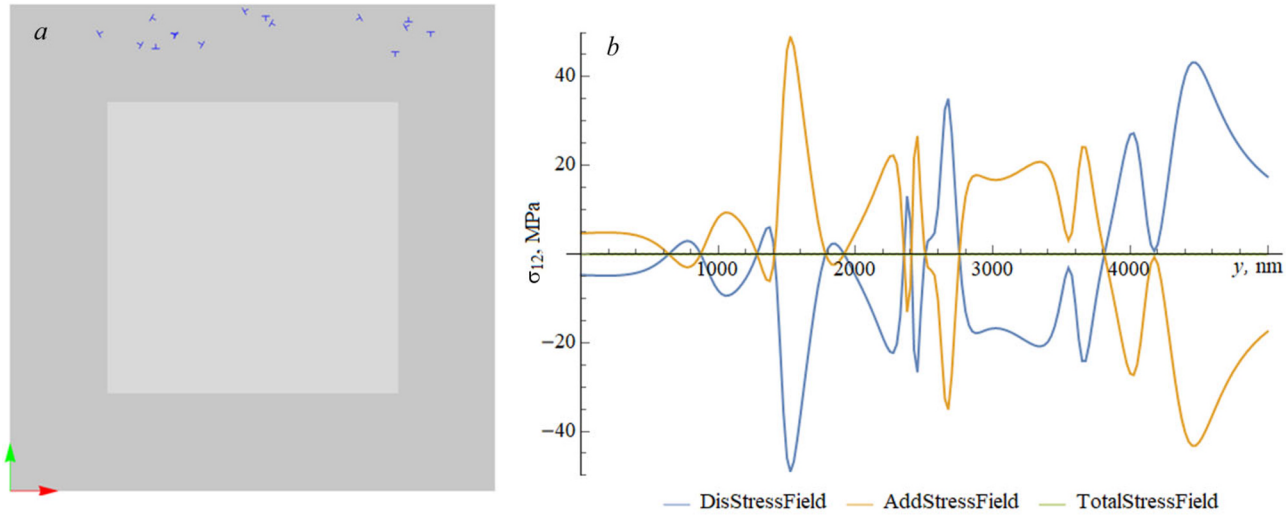

Fig. 3. Illustration of the dislocation distribution in the boundary layer (*a*) and distributions of the σ_{12} components of the dislocation and additional stress fields at the upper boundary (*b*).

Fig. 4. Components of the dislocation stress field, image stress field, and total stress field on the boundaries.

Finally, Figs. 5, 6, and 7 illustrate the evolution of the dislocation structure with the gradual inclusion of the mechanisms of dislocation annihilation, dislocation pinning at obstacles, and dislocation nucleation by sources. In the

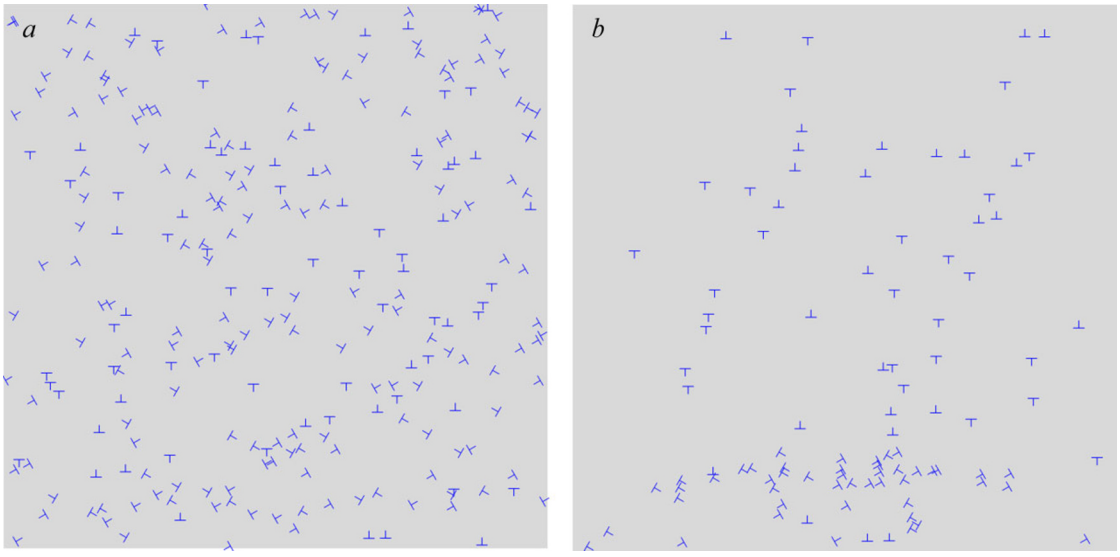

Fig 5. Dislocation structure at the initial time (*a*) and in 50 ns (*b*). The dislocation annihilation mechanism is activated.

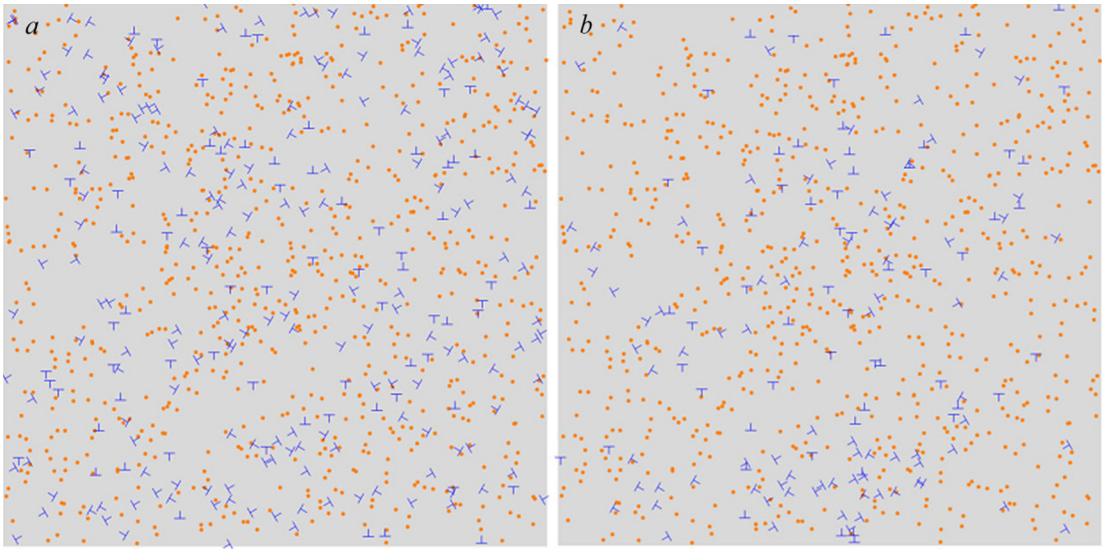

Fig. 6. Dislocation structure at the initial time (*a*) and in 50 ns (*b*). The mechanisms of dislocation annihilation and dislocation pinning at obstacles (indicated by orange points) are activated.

absence of obstacles and dislocation sources in the model, the vast majority of dislocations reach the boundaries, as a result of which the total dislocation density in the single crystal decreases sharply. The appearance of obstacles in the model does not really change the dislocation pattern, although under these conditions, the total dislocation density increases due to the mechanism of dislocation pinning at obstacles. An interesting result is observed in the case of the additional inclusion of the mechanism of dislocation nucleation by sources. In this case, dislocation pile-ups are formed in the lower part of the crystal in several slip planes (the dislocation network structure). It should be noted that the annihilation mechanism in all three experiments is weak, which is very typical for low-temperature deformation.

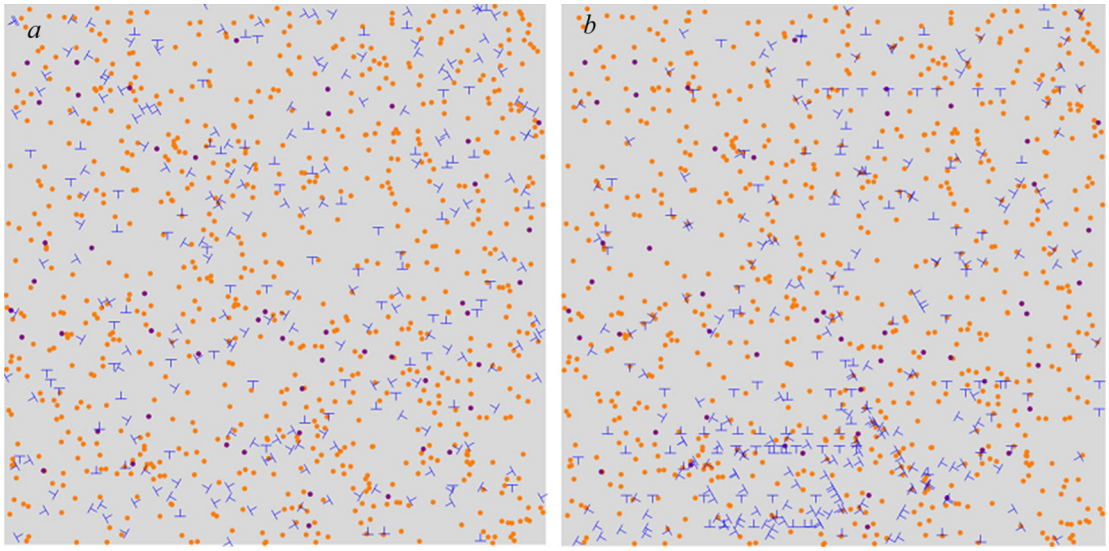

Fig. 7. Dislocation structure at the initial time (*a*) and in 50 ns (*b*). The mechanisms of dislocation annihilation, dislocation pinning at obstacles (indicated by orange points), and dislocation nucleation by sources (indicated by purple points) are activated.

CONCLUSIONS

The paper presents the structure and ratios of the two-dimensional discrete dislocation dynamics model. An analytical derivation of the image field components has been performed in the case of dislocation approaching the boundaries. When the mechanisms of dislocation annihilation, pinning at obstacles, and nucleation by sources are activated, the network dislocation structure is formed in the lower part of the titanium single crystal. The model adequacy tests demonstrated the correctness of the obtained analytical solution for the image fields and the preservation of the actual boundary conditions at each moment of time.

COMPLIANCE WITH ETHICAL STANDARDS

Author contributions

N.A.K. has developed the theoretical formalism and performed the analytical calculations and numerical simulations; N.A.K and P.S.V. contributed to the final version of the manuscript; and P.S.V. supervised the project. All authors have read and agreed to the published version of the manuscript.

Conflicts of interest

The authors declare that they have no known competing financial interests or personal relationships that could have appeared to influence the work reported in this paper.

Funding

This work was funded by the Ministry of Science and Higher Education of the Russian Federation as part of the implementation of the National Project "Science and Universities" within the framework of the State Assignment to the Laboratory of Multilevel Modeling of Structural and Functional Materials of Perm National Research Polytechnic University (Project No. FSNM-2021-0012)

Financial interests

The authors have no relevant financial or non-financial interests to disclose.

Institutional review board statement

Applicable.

REFERENCES

1. A. N. Orlov, Introduction to the Theory of Defects in Crystals [in Russian], Vysshaya Shkola, Moscow (1983).
2. O. B. Naimark, Yu. V. Bayandin, V. A. Leontiev, and S. L. Permyakov, Phys. Mesomech., **8**, No. 5, 21–26 (2005).
3. L. P. Kubin, Dislocation Patterns: Experiment, Theory and Simulation, Plenum Press, New York (1996); DOI: 10.1007/978-1-4613-0385-5_4.
4. G. F. Sarafanov and V. N. Perevezentsev, Patterns of Deformation Grinding of the Structure of Metals and Alloys [in Russian], Publishing House of Nizhny Novgorod State University, Nizhny Novgorod (2007).
5. G. A. Malygin, Adv. Phys. Sci., **169**, No. 9, 979–1010 (1999); DOI: 10.3367/UFNr.0169.199909c.0979.
6. A. N. Gulluoglu and C. S. Hartley, Modell. Simul. Mater. Sci. Eng., **1**, 1–17 (1992); DOI: 10.1088/0965-0393/1/1/001.
7. S. Takeuchi and A.S. Argon, Mater. Sci., **11**, 1542–1566 (1976); DOI: 10.1007/BF00540888.
8. A. N. Gulluoglu and C. S. Hartley, Modell. Simul. Mater. Sci. Eng., **1**, 383–402 (1993).
9. F. Meng, E. Ferrie, C. Depres, and M. Fivel, Int. J. Fatigue, **149**, 106234 (2021); DOI: 10.1016/j.ijfatigue.2021.106234.
10. H. H. M. Cleveringa, E. Van der Giessen, and A. Needleman, Acta Mater., **45**, 3163–3179 (1997); DOI: 10.1016/S1359-6454(97)00011-6.
11. H. G. M. Kreuzer and R. Pippan, Mater. Sci. Eng. A, **400**, 460–462 (2005); DOI: 10.1016/J.MSEA.2005.01.065.
12. L. Nicola, A. F. Bower, K.-S. Kim, *et al*., J. Mech. Phys. Solids, **55**, 1120–1144 (2007); DOI: 10.1016/j.jmps.2006.12.005.
13. Z. Zheng, D. S. Balint, and F. P. E. Dunne, Int. J. Plast., **87**, 1–17 (2016); DOI: 10.1016/j.ijplas.2016.08.009.
14. M. Wallin, W. A. Curtin, M. Rustinmaa, and A. Needleman, J. Mech. Phys. Solids, **56**, 3167–3180 (2008); DOI: 10.1016/j.jmps.2008.08.004.
15. H. M. Zbib, T. D. Rubia, M. Rhee, and J. P. Hirth, J. Nucl. Mater., **276**, 154–165 (2000); DOI: 10.1016/S0022-3115(99)00175-0.
16. E. Van der Giessen and A. Needleman, Modell. Simul. Mater. Sci. Eng., **3**, 689–735 (1995); DOI: 10.1088/0965-0393/3/5/008.
17. J. Hirth and J. Lothe, Theory of Dislocations, John Wiley & Sons, New York (1982).

18. W. Cai, A. Arsenlis, C. R. Weinberger, and V. V. Bulatov, J. Mech. Phys. Solids, **54**, 561–587 (2006); DOI: 10.1016/j.jmps.2005.09.005.
19. M. Tang, W. Cai, G. Xu, and V. V. Bulatov, Modell. Simul. Mater. Sci. Eng., **14**, 1139–1151 (2006); DOI: 10.1088/0965-0393/14/7/003.
20. K. Balusu and H. Huang, Modell. Simul. Mater. Sci. Eng., **25**, 035007 (2017); DOI: 10.1088/1361-651X/aa5a9d.